Journal of Luminescence 293 (2026) 121800

Contents lists available at ScienceDirect

Journal of Luminescence

journal homepage: www.elsevier.com/locate/jlumin

Full Length Article

First-principles calculations of the structural, electronic, elastic and thermodynamic properties of $MgAl_2O_4$:Ti^{3+} and $ZnAl_2O_4$:Ti^{3+}

Andrei Chesnokov [a,*], Denis Gryaznov [b], Yang Wang [a], Alise Podelinska [c], Evgeni Shablonin [c], Aleksandr Lushchik [c], Pieter Dorenbos [d], Mikhail G. Brik [a,c,e,f,g,*]

[a] School of Integrated Circuits, Chongqing University of Posts and Telecommunications, Chongqing, 400065, China
[b] Institute of Solid State Physics, University of Latvia, Kengaraga 8, Riga, LV-1063, Latvia
[c] Institute of Physics, University of Tartu, W. Ostwald Str. 1, Tartu, 50411, Estonia
[d] Delft University of Technology, Faculty of Applied Sciences, Department of Radiation Science and Technology, Mekelweg 15, 2629 JB, Delft, Netherlands
[e] Centre of Excellence for Photoconversion, Vinča Institute of Nuclear Sciences – National Institute of the Republic of Serbia, Poštanski fah 522, 11001, Beograd, Serbia
[f] Faculty of Science and Technology, Jan Długosz University, Armii Krajowej 13/15, 42–200, Częstochowa, Poland
[g] Academy of Romanian Scientists, 3 Ilfov, 050044, Bucharest, Romania

ARTICLE INFO

Keywords:
DFT
Spectroscopy
Crystal field
Electronic levels
MAO(MAS)
ZAO(ZAS)

ABSTRACT

Detailed first-principles calculations of structural, electronic, elastic, thermodynamic and vibrational properties of two spinel crystals, $MgAl_2O_4$ (MAO) and $ZnAl_2O_4$ (ZAO): neat and doped with Ti^{3+} ions, at ambient and elevated hydrostatic pressure, are reported. Special attention is given to the location of Ti^{3+} 3d level in the hosts' band gap. Various exchange-correlation functionals are employed for that purpose; the best agreement with the experimental data is obtained for the M06 functional, which places the Ti^{3+} state at 4.39 eV above the valence band top in $MgAl_2O_4$ and at 4.08 eV in $ZnAl_2O_4$. Crystal field splitting of the Ti^{3+} 3d states is calculated for different pressures; dependence of the crystal field strength 10Dq on pressure and Ti^{3+}–O^{2-} distance is analyzed. Our calculations of the Debye temperature (based on the knowledge of elastic constants) result in close agreement with the corresponding experimental data.

Doping with Ti^{3+} ions leads to a slight decrease of the elastic parameters and lowering the Debye temperature by 20–40 K, because the Ti^{3+}–O^{2-} chemical bonds become longer and softer when compared with the Al^{3+}–O^{2-} ones in undoped materials. As a result, slight red shift of the most prominent features in the vibrational spectra is expected; this is confirmed by the performed calculations. Obtained results give a deeper insight into the properties of doped optical materials, highlight the effect of added impurity ions on their physical parameters and may serve as useful guides for smart materials engineering with wide opportunities of fine tuneability of their most important characteristics for potential applications.

1. Introduction

Crystals with the spinel structure constitute a very large family of compounds with the general chemical formula AM_2X_4, where *A* and *M* are the metal cations occupying the four- and six-fold coordinated positions, respectively, and *X* stands for the anion, which can be any of these elements: oxygen, sulfur, selenium, tellurium, nitrogen. As a rule, the oxidation states of the *A* and *M* cations are +2 and +3, respectively, although the +4 oxidation state for the second cation can be met (in such a case, the general chemical formula is A_2MX_4) [1,2]

The name "spinel" was given to $Mg_2Al_2O_4$ mineral in 1779 by the Belgian scientist Jean Démeste (1743 – 1783) [3,4]. It originates from the Latin word "spinella" (a little thorn), due to its sharp octahedral crystals. A large number of possible combinations of cations and anions determines a wide variety of spinel crystals with different physical properties. In addition, it is also possible to make the solid solutions having the spinel structure, with a partial or complete cation substitution, thus increasing the number of spinel compounds and allowing for fine tunability of their properties by varying chemical composition.

All spinel crystals can be divided into the so-called "normal" $A(M_2)X_4$ and "inverse" $M(AM)X_4$ spinels, with the ions in the parenthesis being located at the octahedral sites [5]. Intermediate cases can often happen; they can be generally described as $A_{1-\lambda}M_{\lambda}(A_{\lambda}M_{2-\lambda})X_4$ with λ characterizing the degree of inversion ($\lambda=0$ for the normal spinels and $\lambda=1$ for the inverse ones). The anion fractional coordinate *u* in the spinel structure depends strongly on the cation inversion parameter [6].

* Corresponding authors.
E-mail addresses: andrejs.cesnokovs@cfi.lu.lv (A. Chesnokov), mikhail.brik@ut.ee (M.G. Brik).

https://doi.org/10.1016/j.jlumin.2026.121800
Received 9 November 2025; Received in revised form 9 February 2026; Accepted 9 February 2026
Available online 16 February 2026

Table 1
Structural properties of the spinels considered in the present work.

	MAO Exp.	Calc.	ZAO Exp.	Calc.	MAO:Ti^{3+} Calc.	ZAO:Ti^{3+} Calc
Lattice parameters, Å	a = 8.075[a]	8.1527[b], 8.15[c], 8.030[d], 8.034[e]	a = 8.0876[f]	8.1534[b], 8.172[g], 7.98[h], 8.321[i]	a = 8.1852[b] b = 8.1725 c = 8.1915	a = 8.18399[b] b = 8.18399 c = 8.18396
Cell volume V, $Å^3$	526.54[a]	541.878[b], 541.343[c], 517.782[d], 518.556[e]	529.004[f]	542.027[b], 545.83[g], 508.170[h], 576.138[i]	548.375[b]	548.138[b]
O position parameter x	0.264[a]	0.26424[b]	0.375[f]	0.38995[b]	—	—

[a] Ref.[38] ; [b] This work; [c] Ref.[21] ; [d] Ref.[45] ; [e] Ref.[46] ; [f] Ref.[39] ; [g] Ref.[47] ; [h] Ref.[48] ; [i] Ref.[49] .

Spinels are not only abundant in nature, but they can also be made artificially, in the form of single crystals, ceramics or powders, with addition of different transition metal or rare earth ions, to be used as phosphor materials with applications in lighting, optical thermometry etc. Some recent representative examples are $MgAl_2O_4$:Tb^{3+} [7], $ZnGa_2O_4$:Ce^{3+}, Tb^{3+}, Eu^{3+} [8], $MgAl_2O_4$:Ce^{3+} [9], $ZnAl_2O_4$ and $ZnGa_2O_4$ with Cr^{3+} [10], $Mg_{1-x}ZnxAl_2O_4$:Cr^{3+} [11], $MgAl_2O_4$:Ni_2^+ [12], $MgAl_2O_4$:Ti_3^+ [13,14], $ZnAl_2O_4$:Ti_3^+ [15] etc. Neat spinels also find important technological applications. Thus, high radiation resistance and low swelling even after the exposure to high fluence of fast neutrons encouraged the long-term use of $MgAl_2O_4$ in different nuclear technologies [16].

Among various impurities that can be introduced into the spinel matrices, the Ti^{3+} ions as dopants in spinels are of special interest. They substitute for the trivalent cation at the octahedral sites. Since Ti^{3+} ions have a single-electron configuration ($3d^1$), they are ideal model systems to be studied by the first-principles calculations, because no multielectron effects within the 3d electron configuration can arise in this case.

In the present paper we consider two spinel crystals, $MgAl_2O_4$ (MAO) and $ZnAl_2O_4$ (ZAO), neat and doped with the Ti^{3+} ions. By performing systematic first-principles calculations of their structural, electronic, elastic and thermodynamic properties we analyze the influence of the A cation and impurity ion on all these properties of the host materials at the ambient and elevated hydrostatic pressure. Special attention was paid to the location of the Ti^{3+} 3d states in the hosts' band gap. A thorough analysis of trigonal deformations of the TiO_6 allowed to identify a criterion that determines the symmetry properties and degeneracy of the ground Ti^{3+} electronic state. All obtained results — whenever possible — are compared with the corresponding experimental and/or literature data.

The structure of the paper is as follows: Section 2 contains description of the method of calculation; all obtained results are presented in Section 3 and its subsections, and Section 4 concludes the paper with a short summary of the main findings.

2. Method of calculations

Density functional calculations (DFT) in the formalism of linear combination of atomic orbitals were performed with tools implemented in the CRYSTAL23 software [17,18]. The hybrid B3LYP exchange-correlation functional with Vosko-Wilk-Nusair correlation potential [19,20] and all-electron basis sets of atomic Gaussian functions were chosen to build up on and to continue the work on by Platonenko *et al.* [21]. All-electron basis sets were taken from the CRYSTAL database of basis sets [22]: 8s-511sp for Mg [23]; 8s-64111sp-41d for Zn from [24] with modified exponents from [25,26]; 8s-511sp-1d for Al [27]; 8s-411sp for O [28]; 8s-6411sp-11d for Ti [29,30]. Full basis sets are listed in the Supporting Information (SI).

Properties of pure MAO and ZAO crystals were modeled in their respective primitive unit cells. The Ti^{3+} ions were added to cubic 56-atom conventional cells. The Brillouin zone was sampled with Γ-centered k-point meshes generated with the Monkhorst-Pack [31] scheme according to the supercell (SC) size. In convergence tests computed for the primitive cell a $8 \times 8 \times 8$ mesh turned out to be optimal. For the cubic 56-atom cells $4 \times 4 \times 4$ mesh was used. All calculations involving Ti ions were spin-polarized.

In CRYSTAL calculations five parameters control the numerical accuracy of computing two-electron integrals. Throughout all calculations in this work they were set to 9 9 9 9 18. Physical interpretation of these values is given in [17] and in the SI. All calculations with the Ti ion were spin-polarized. In all calculations the convergence criterion for self-consistent field procedure was set to 10^{-10} Hartree. In all geometry relaxation calculations, in addition to the previous criteria, the root-mean-squares of the gradient and of the displacement were set to 3×10^{-5} and 12×10^{-5} a.u., respectively.

The structures were tested for stability by performing Γ-point frequency calculations [32,33]. Elastic properties and structural relaxations under pressure were calculated using the approach outlined in Refs. [34,35]. In these calculations the default convergence thresholds were used.

3. Results and discussion

3.1. Structural properties

The initial structural data were taken from the Open Crystallography Database [36,37], where original sources for MAO and ZAO crystals are [38] and [39], respectively. The crystalline symmetries of MAO and ZAO are described by space group 227 ($Fd\bar{3}m$). Their respective primitive cells are trigonal and contain 14 atoms, or two formula units. Spinel's conventional cell is a face-centered cubic cell that consists of four primitive cells and has eight formula units. In their conventional cells (with conventional choice of origin), the Mg or Zn atoms occupy Wyckoff positions 8a ((1/8 1/8 1/8), point group T_d); the Al atoms are in positions 16d ((1/2 1/2 1/2), point group D_{3d}), and the O atoms occupy the 32e positions (x x x, point group C_{3v}). The following linear transformation transforms spinel's primitive cell into its smallest conventional cell:

$$\begin{bmatrix} -1 & 1 & 1 \\ 1 & -1 & 1 \\ 1 & 1 & -1 \end{bmatrix}. \quad (1)$$

The same transformation reduces the $Fd\bar{3}m$ group to its subgroup $P\bar{4}3m$ (No. 215), and as a consequence the occupied Wyckoff orbits are split [40,41]. Specifically, the 16d orbit (occupied by Al atoms, point group D_{3d}) splits into orbits 12i and 4e, whose respective point groups are C_s and C_{3v} (corresponding site symmetries are $..m$ and $.3m$). Applications of Wyckoff splitting to computational modeling of materials including MAO are described in earlier publications [42,43].

Effects of doping with the Ti^{3+} ions were modeled by optimizing the crystal structures with one Al^{3+} ion replaced by one Ti^{3+} ion in one unit

cell. Although such dopant concentration (one out of sixteen atoms in a unit cell, or 6.25%) is somewhat higher than the experimental values (which are rarely above 3%), it still allows to get valuable information about the structural and electronic properties of the TiO_6 octahedra and compare them to AlO_6 octahedra in the studied compounds. We model a neutrally charged defect in an uncharged cell, therefore our Ti-Ti distances of at least 8.18 Å in either direction are well within the 5–10 Å threshold necessary to recover the macroscopic bulk behavior for electrostatic screening or elasticity to within 0.01 eV [44]. This is the smallest possible supercell for such calculations. The next smallest supercell is a $2 \times 2 \times 2$ expansion of the primitive cell, which has 112 atoms, twice as many as our cell. While that cell allows to model 3.125% concentration of Ti, it also doubles the number of electrons, making DFT calculations 8 times as demanding.

Table 1 collects the summary of the experimental and optimized structural data for the MAO and ZAO crystals, both neat and doped with Ti^{3+} ions.

Our lattice constants are in good agreement with the experimental results. They are also in the range of lattice constants calculated for the title hosts in other references by using different functionals. Replacement of a Al^{3+} ion by a larger Ti^{3+} ion is accompanied by a slight increase of the optimized lattice constants of the doped materials in comparison with the pure spinels.

Splitting of Wyckoff positions in spinel supercells means that there are only two different ways to perform Al → Ti substitution that conserves, at least in part, crystalline symmetry of spinel. In our calculations we observed that in ZAO the choice of substitution site does not affect the energy of defect's formation, evidenced by negligible differences of ca. 0.5 μeV in total energies of Ti-doped ZAO cells.

In MAO the same substitution converged to different results, depending on the substituted Al site. An initial relaxation at the 12i site (point group C_s) produced unstable solution with an imaginary vibrational frequency. This result also had an electronic ground state different from that in ZAO:Ti. In Zn spinel Ti's occupied 3d level was triply degenerate (t_{2g}), while in MAO:Ti it was doubly degenerate. This reminded us of a result by Landron and Lepetit [50]: in their study they observed that trigonal distortion of the regular octahedron along the [111] direction affects the relative energies of t_{2g} orbitals, i.e. they split into two degenerated e' orbitals and one a_{1g} orbital.

Therefore, when we obtained a t_{2g} solution for MAO:Ti, we subjected it and the same configuration of ZAO:Ti to a geometrical test: two axial oxygen atoms in the TiO_6 octahedron were symmetrically shifted along a circular arc in the $(1\,\bar{1}\,0)$ plane (effectively, changing the O_{axial}–Ti–[111] angle). For both spinels it was found that small changes of ca. ±6° carry a small penalty in total energy, <1 eV above the ground state, Fig. 1. In MAO this distortion led to a small energy decrease, which was still higher in energy than the imaginary-mode solution. The true ground state for MAO:Ti was found by following the imaginary mode. Fig. 2 summarizes relationships between different solutions for Al → Ti substitution in MAO.

3.2. Electronic properties: A brief summary of the experimental spectroscopic data

In spite of wide applications of the MAO crystals, its several fundamental optical characteristics are not precisely determined yet. In particular, this applies to the energy gap value E_g, excitonic states and optical absorption of intrinsic cation lattice defects, or the so-called antisite defects (ADs), representing the situation when the Mg^{2+} and Al^{3+} ions swap their sites. Due to low formation energy of $Mg|_{Al}$ and $Al|_{Mg}$ (both defects are charged with respect to a regular lattice), these defects are easily detectable even in pristine, as-grown crystals and allow to accommodate radiation-induced disorder of cation sublattice [51–54]. The energy levels of such defects can appear in the host's band gap close to the conduction band bottom, thus masking the true host-related absorption edge.

Thorough spectroscopic measurements can help in estimations of the experimental band gap values of crystalline materials. Cathodoluminescence spectroscopy of pristine MAO single crystals revealed several lines/bands connected with the traces of impurity ions (e.g., *R*-components of the Cr^{3+} ions) and broadband UV emission, a maximum of which at low temperatures is located from 5.3 to 5.8 eV depending on inversion parameter of as grown materials interpreted as the luminescence of self-trapped excitons or radiative recombination of electron-hole (e-h) pairs at intrinsic lattice defects (e.g., ADs) [55–57].

The intrinsic luminescence of MAO centered at the 5.3 eV has main excitation bands at ~7.2 and ~8 eV [57]. To sum up these experimental findings, we conclude that the energy gap in the stoichiometric $MgAl_2O_4$ single crystals at low temperatures can be estimated as $E_g = 8.2$ eV. This value is between the relevant ones in MgO (7.8 eV) and α-Al_2O_3 (9.4 eV) binary oxides, the equimolecular mixture of which forms a stoichiometric $MgAl_2O_4$ spinel crystal. Additionally, Ref. [58] also gives the estimation of the experimental band gap of MAO crystal between 8.05 and 8.2 eV.

Information about the ZAO band gap is even more scarce. The intrinsic UV emission of ZAO single crystals is peaked at lower energies (at about 4.9 eV) if compared with the MAO spinel, which agrees with the energy gap values E_g in these materials. The substitution of Mg^{2+} ions by Zn^{2+} ions (having a greater atomic number and ionic radius) reduces the band gap value at least by 1 eV. According to Ref. [59], the edge of fundamental absorption lies above 6.05 eV, but such intrinsic absorption definitely involves the region of exciton states as well. The location of the exciton band in ZAO nanofibers is expected to be at about 7 eV [60], which allows to estimate the ZAO band gap as 7 eV or slightly higher.

3.3. Electronic properties: First-principles calculations

Fig. 3 shows the calculated band structures of neat MAO and ZAO single crystals.

Both crystals are indirect band gap materials, with calculated band gaps of 7.73 eV (MAO) and 6.45 eV (ZAO). Electronic band structures of Ti^{3+}-containing MAO and ZAO crystals are shown in Fig. 4. Decreased ZAO band gap obtained in our calculations agrees with the above given experimental results and with slightly increased ZAO lattice constants and corresponding interatomic distances, if compared with the MAO data. Tops of valence bands in both materials (made mainly by the oxygen 2p states) are remarkably flat, which indicates a low mobility of the holes in the valence band, whereas the lowest states from the conduction bands (composed by the cations unoccupied orbitals, 3s states of Mg, 3s, 3p states of Al, and 4s states of Zn) exhibit considerable dispersion, especially around the Γ point. Some other calculated results available in the literature (for MAO 7.8 eV [61], 7.4 eV [62], for ZAO 4.25 eV [63], 4.44 eV [51]) are consistent with our values. Lower values of the band gaps for ZAO obtained by other authors are explained by using the GGA functional, which always underestimates the true band gap.

The most important result of incorporation of impurity ions into a crystalline solid is a formation of additional energy levels in the host's band gap, which is confirmed by the data shown in Fig. 4. The zero of energy in Fig. 4 is placed at the lowest occupied 3d state of Ti^{3+}, which is 3.90 eV above the top of the valence band in MAO and 3.66 eV in ZAO.

This value is close to the previously reported for Al_2O_3:Ti^{3+} (4.78 eV, according to the calculations in Ref. [64]). Experimental estimations of the ground states of transition metal ions in insulating hosts can be made based on the charge transfer transitions. Thus, the value of 4.8 eV for the Ti^{3+} in MAO was reported in Ref. [65]. As for the ZAO:Ti^{3+}, the experimental measurements of the valence band — Ti^{4+} charge transfer transition [66] place the Ti^{3+} ground state at about 5 eV above the valence band top. Both experimental values (given the accuracy of

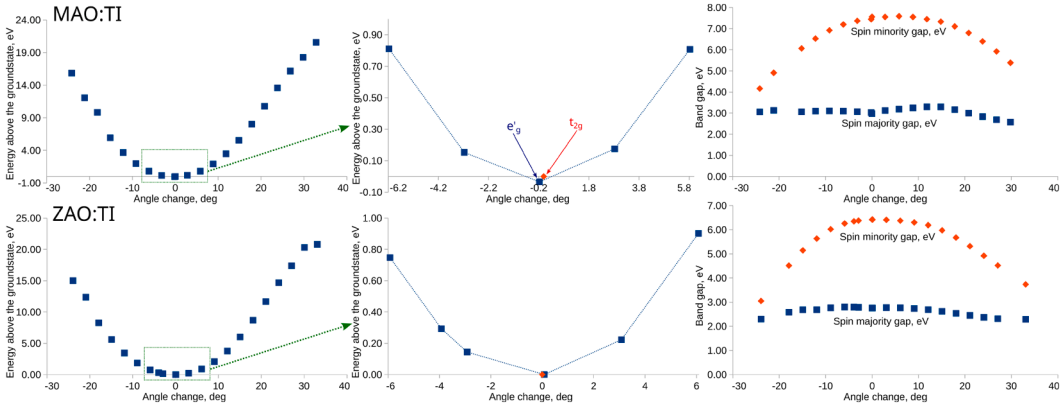

Fig. 1. Effects of O_{axial}–Ti–[111] angle change in TiO_6. Top row: MAO:Ti. Bottom row: ZAO:Ti. Left to right: total energy; a fragment of the energy diagram, showing small angle changes, corresponding to <1 eV increases in the total energy; band gaps. A small decrease in total energy is associated with a small angular displacement. Here, "ground state" refers to a t_{2g} starting point.

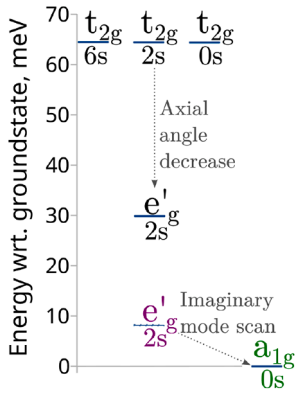

Fig. 2. Different solutions to relaxation of MAO:Ti. 6s, 2s and 0s are the number of symmetry operations. Labels of electronic orbitals indicate whether the t_{2g} level splits, and if so, which orbital is lower in energy.

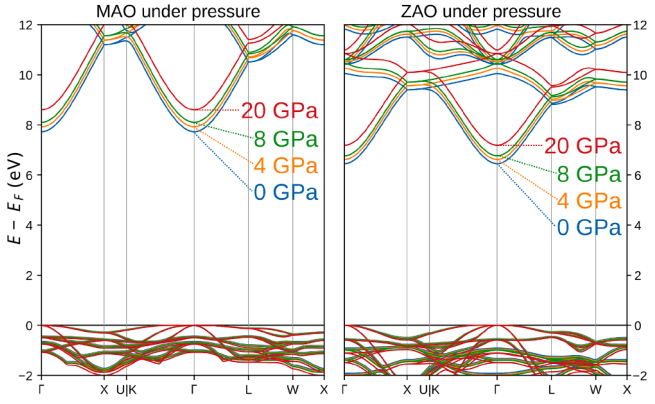

Fig. 3. Calculated band structures of neat MAO (left) and ZAO (right) single crystals under pressure.

measurements and calculations) are in reasonable agreement with the values calculated in the present work.

Splitting of the Ti^{3+} 3d states into the t_{2g} (ground state) and e_g (excited state) in a crystal field is clearly seen in Fig. 4; the separation between them is the crystal field strength 10Dq, which in both cases is about 4.1 eV. This value overestimates the experimentally determined 10Dq parameter for MAO:Ti^{3+} (20041 cm^{-1} or 2.48 eV [67]).

Basic definition of the 10Dq parameter in the classical crystal field theory is the energy interval between the t_{2g} and e_g orbitals of the central ion located in the ideal octahedral crystal field with O_h local symmetry. However, direct and straightforward application of this definition to the vast majority of real systems can be hindered by at least two facts: i) low symmetry splitting of both t_{2g} and e_g states, which may result in additional structured bands in the absorption/emission spectra and formation of up to five 3d energy levels in the case of low enough local symmetry (all point groups with only one-dimensional irreducible representations), and ii) high degree of delocalization of 3d electrons because of their strong interaction with ligands and overlap of 3d wave functions with the s, p states of ligands (in our case, 2s, 2p states of oxygen).

The latter implies that the 3d states of an impurity ion are no longer atomic-like states with purely 3d character but contain a considerable contribution of the ligands' states. Both above-mentioned reasons are present in the studied spinels. We emphasize that in our calculations (ground state DFT) computed e_g states in conduction band are not localized states. These delocalized e_g states are bound to other states in the conduction band which are not true excited states by definition of the ground state DFT, and thus computed barycenters of t_{2g} and e_g orbitals may not correspond exactly to observed energies of optical transitions. Alternatively, 10Dq may be defined as the first d–d excitation. This value may be approximated by difference between two differently occupied d levels in the band structure. Under this definition our value for 10Dq differs from experimental value by ca. 0.5 eV. This definition works well for ZAO:Ti, but it does not work for MAO:Ti, where the t_{2g} level splits into a_{1g} and $e\}_g$ levels, and the aforementioned limitations of DFT also apply here. Regardless of the definition, computed value of 10Dq depends on the choice of DFT functional, as will be shown further, and thus the main utility of these calculations lies in the ability to see how factors such as applied pressure or changes in composition affect this value.

Our process for calculating value of 10Dq is shown schematically in the right part of Fig. 4. It involves calculating centers of DOS signals and, in case of MAO:Ti, centers of sums of DOS signals. Center c of a DOS signal ranging from a to b is defined as a point between a and b which satisfies the following equation:

$$\int_a^c DOS\, dE = \int_c^b DOS\, dE. \tag{2}$$

Crystalline structure optimization and calculations of electronic properties were also performed at the elevated hydrostatic pressures in the range from 0 to 20 GPa. The band gaps and the crystal field strength parameter 10Dq of both crystals are linearly increasing with pressure, as indicated by Fig. 5. In Ti-doped spinels the magnitude of band gap is determined by the position of Ti $3d^1$ level, and while energy of $3d^1$ level is affected by changes in pressure (see Fig. 6), magnitude of the

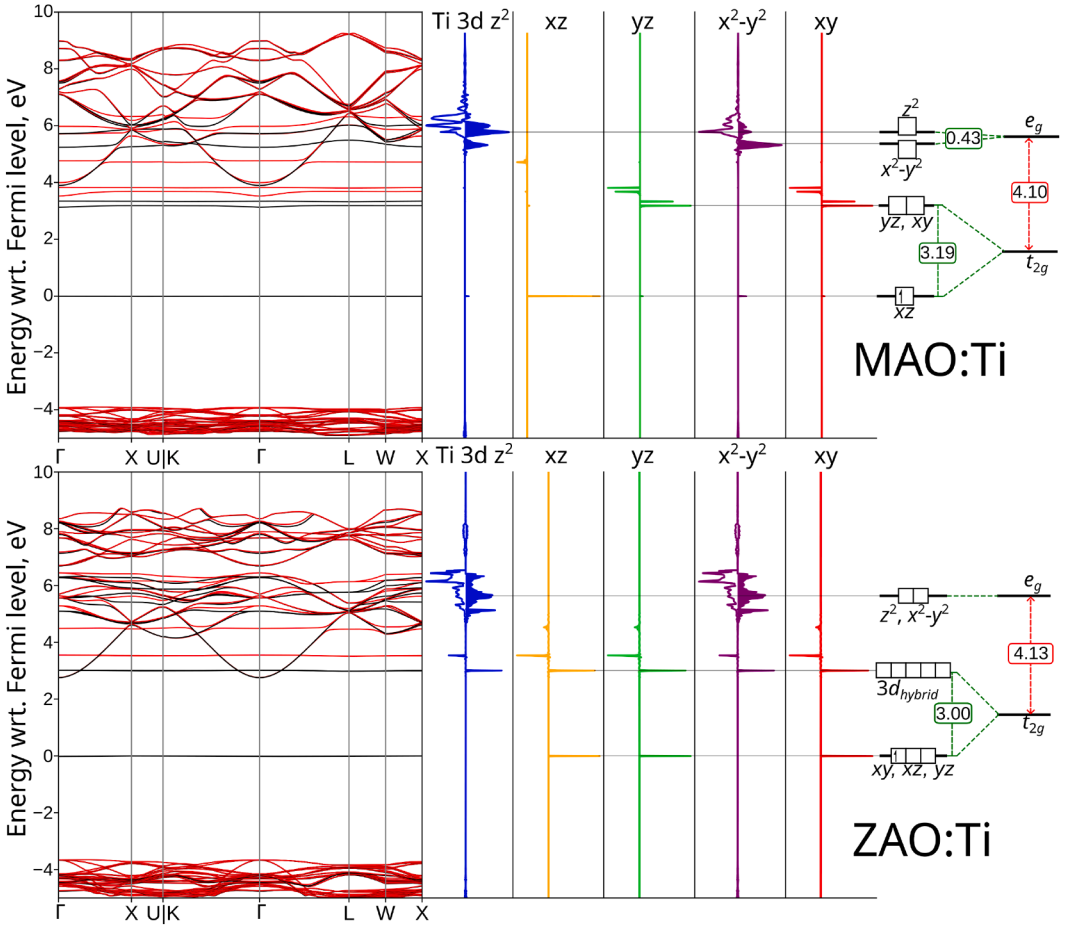

Fig. 4. Calculated band structures of Ti^{3+}-doped MAO (top) and ZAO (bottom) single crystals. Black and red lines in band structure diagrams are spin majority and spin minority respectively. DOS signals left of the vertical line are spin-down (spin minority); those on the right are spin-up (spin majority). Shaded areas in DOS plots represent integration limits for calculating centres of peaks (shown in horizontal gray lines). Rightmost diagrams illustrate method for evaluating the crystal field splitting parameter 10Dq.

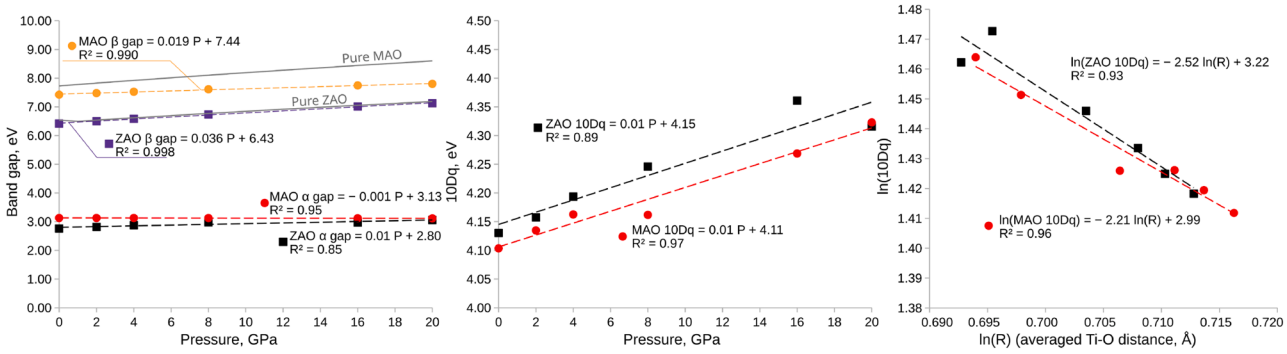

Fig. 5. Calculated pressure dependencies of band gaps (left), 10Dq (center), and ln(10Dq) in pure and Ti^{3+}-doped MAO and ZAO. Dashed lines represent linear fits. Equations of fit are given for each line. Gaps and 10Dq are expressed in eV, pressure is in GPa. Solid grey lines represent band gaps in pure spinels. Data for reproducing this figure are in the SI.

associated band gap remains almost constant, requiring large structural distortions to change, cf. Fig. 1, where spin majority gap (α gap in Fig. 5) also remains almost constant in response to structural changes. This is in stark contrast to spin minority gap (β gap), which is largely determined by changes in host's conduction band (see Fig. 3).

In crystal field theory 10Dq is inversely proportional to ligands' distance from the central ion: $10Dq = A/R^n$, where R is Ti–O distance (averaged over the TiO_6 octahedron), and A is constant. Logarithm of this expression yields $\ln(10Dq) = \ln(A) - n\ln(R)$. From fits in Fig. 5, we obtain $n_{MAO} = 2.21$, and $n_{ZAO} = 2.52$.

Additionally, test calculations for MAO:Ti^{3+} and ZAO:Ti^{3+} were performed to investigate the influence of various functionals available in the used software on the calculated properties of impurities. Fig. 6 shows variation of the Ti^{3+} 3d level position in band gap of both spinels under different exchange-correlation functionals and with applied hydrostatic pressure.

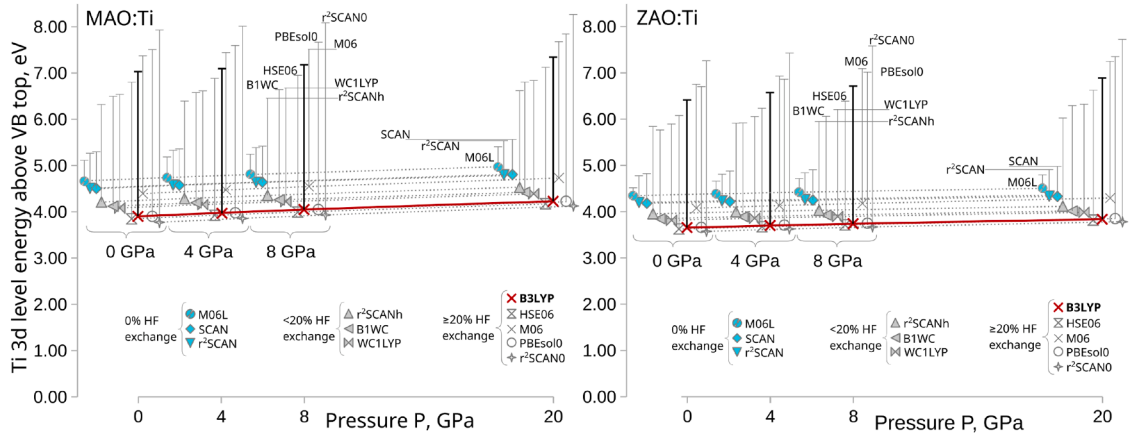

Fig. 6. Variation of the Ti^{3+} 3d level position in band gaps of both crystals depending on the choice of various DFT functionals and with applied hydrostatic pressure. Error bars represent distance from the Ti level to the bottom of conduction band. Data for reproducing this figure are in the SI.

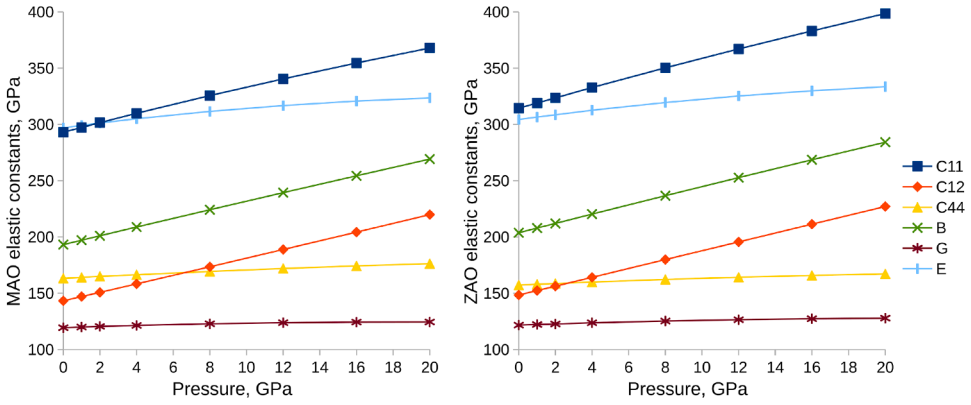

Fig. 7. Calculated pressure dependencies of the elastic constants for neat MAO (left) and ZAO crystals (right). The calculated values are shown by symbols, the linear fits are solid lines. Equations of fits are given in Table 2. Data for reproducing this figure are in the SI.

According to calculations of charge transition level (CTL) energies in [65], $Ti^{4+/3+}$ CTL energy in MAO is 4.8 eV above VB and 3.45 eV below CB. Some of the tested DFT functionals yield band structures close to this model. Pure HF functionals (M06L [68], SCAN [69], r2SCAN [70]) place Ti^{3+} level above VB at 4.67, 4.50, and 4.51 eV accordingly, but too close to CB: less than 1 eV in all cases. Results obtained with hybrid meta-GGA M06 functional with 27% exact exchange [71] are closest to these values among all tested functionals: without external pressure they place Ti^{3+} level at 4.39 eV above VB and 2.98 eV below CB. Another good compromise is obtained with relatively simpler hybrid GGA functionals B3LYP (20% HF) and PBESOL0 (25% HF) [72]; both place Ti^{3+} level at 3.90 eV above VB, and 3.13 eV (B3LYP) or 3.60 eV (PBESOL0) below CB.

3.4. Elastic and thermodynamic properties: First-principles calculations

Since both MAO and ZAO crystals have cubic structure, their elastic properties are described by a 6×6 matrix of elastic constants C_{ij} with only three independent constants C_{11}, C_{12}, C_{44}. Calculations of elastic properties for both neat and Ti-doped MAO and ZAO crystals were performed for ambient and elevated hydrostatic pressures; the obtained results are summarized in Tables 2–4 and Fig. 7.

Application of the external pressure makes chemical bonds stiffer; as a result, the values of all elastic constants are increasing. Table 2 collects the linear approximations of the calculated elastic constants (shown by symbols in Fig. 7) for undoped MAO and ZAO spinels.

Table 2
Linear approximations of elastic properties of the spinels considered in the present work (equations of straight lines from Fig. 7). P is the external hydrostatic pressure in GPa ($0 \le P \le 20$), the calculated result is also in GPa.

Elastic constants, GPa	MAO	ZAO
C_{11}	$294.18 + 3.76P$	$315.34 + 4.23P$
C_{12}	$143.07 + 3.82P$	$148.41 + 3.93P$
C_{44}	$163.59 + 0.66P$	$157.68 + 0.50P$
Bulk modulus B	$193.44 + 3.81P$	$204.05 + 4.03P$
Shear modulus G	$119.99 + 0.26P$	$122.15 + 0.32P$
Young modulus E	$298.69 + 1.36P$	$305.86 + 1.49P$

Another way of extracting the values of bulk modulus and its pressure derivative for a crystalline solid is the optimization of crystal structure at different pressures with subsequent fit of the unit cell volume change to various equations of state (EOS). This was done using automated routines in CRYSTAL by varying the volumes of fully relaxed cells in range from 80% to 120% [35]. Following four equations of state [17] were fitted to the obtained volume-energy pairs: Murnaghan's EOS

$$P(V) = \frac{B_0}{B_0'}\left[\left(\frac{V_0}{V}\right)^{B_0'} - 1\right], \tag{3}$$

third-order Birch-Murnaghan's EOS

$$P(V) = \frac{3B_0}{2}\left[\left(\frac{V_0}{V}\right)^{\frac{7}{3}} - \left(\frac{V_0}{V}\right)^{\frac{5}{3}}\right]\left\{1 + \frac{3}{4}(B_0' - 4)\left[\left(\frac{V_0}{V}\right)^{\frac{2}{3}} - 1\right]\right\}, \tag{4}$$

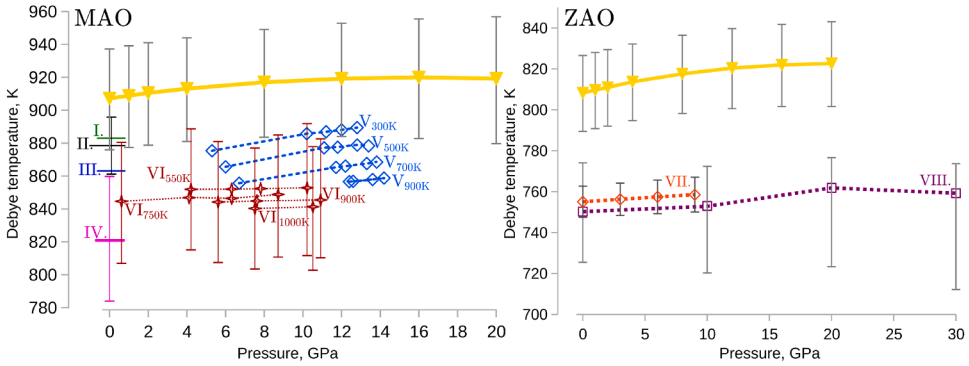

Fig. 8. Calculated Debye temperatures for neat MAO and ZAO crystals. Results from the present investigation are shown in continuous yellow line, upper and lower bounds are due to Voigt and Reuss definitions of the shear modulus, respectively. The Roman numerals I—VIII are literature data. I:[76]; II:[74]; III:[77,78]; IV:[79–81]; V:[75]; VI:[82]; VII:[83]; VIII:[47]. See SI for a complete description.

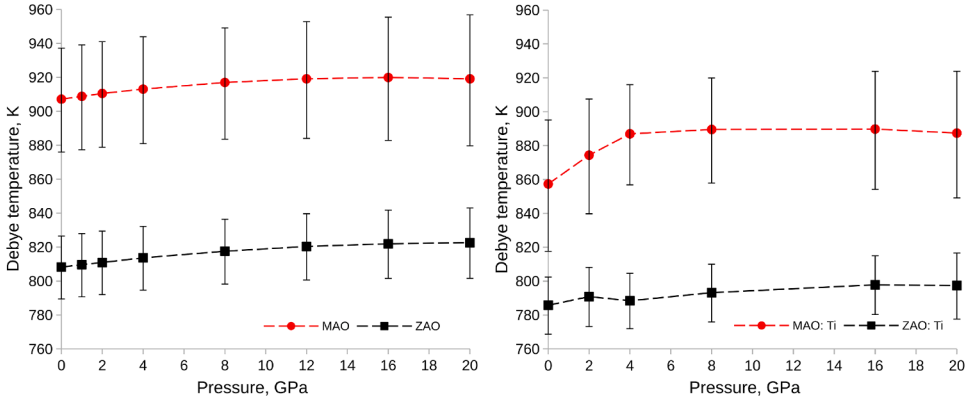

Fig. 9. Debye temperature as function of applied pressure. Left: pure MAO and ZAO spinels. Right: Ti-doped spinels, upper and lower bounds are due to Voigt and Reuss definitions of the shear modulus, respectively. Data for reproducing this figure are in the SI.

Table 3
Minimum volumes[a], bulk moduli and their first derivatives according to EOS fits in pure spinels.

	MAO			ZAO		
EOS	V_0, Å^3	B, GPa	B'	V_0, Å^3	B, GPa	B'
Murnaghan	541.88	192.68	3.92	542.48	200.92	4.07
Birch-Murnaghan	541.88	193.27	3.95	542.24	203.40	4.18
Poirer-Tarantola	541.88	193.74	3.96	542.08	206.09	4.26
Vinet	541.88	193.51	3.96	542.16	204.61	4.23

[a] Calculated in primitive cells, presented here re-scaled to match crystallographic cells

Table 4
Results of EOS fits for Ti-doped spinels.

	MAO:Ti			ZAO:Ti		
EOS	V_0, Å^3	B, GPa	B'	V_0, Å^3	B, GPa	B'
Murnaghan	548.54	188.87	3.86	548.63	197.87	4.10
Birch-Murnaghan	548.34	191.08	3.96	548.40	200.33	4.22
Poirer-Tarantola	548.22	193.00	4.01	548.21	203.07	4.30
Vinet	548.26	192.02	4.00	548.29	201.54	4.27

Poirier-Tarantola's EOS

$$P(V) = B_0 \frac{V_0}{V}\left[\ln\left(\frac{V_0}{V}\right) + \frac{B_0' - 2}{2}\left[\ln\left(\frac{V_0}{V}\right)\right]^2\right], \quad (5)$$

and Vinet's EOS

$$P(V) = 3B_0\left(\frac{V}{V_0}\right)^{-\frac{2}{3}}\left[1 - \left(\frac{V}{V_0}\right)^{\frac{1}{3}}\right]\exp\left[-\frac{3}{2}(B_0' - 1)\left[\left(\frac{V}{V_0}\right)^{\frac{1}{3}} - 1\right]\right]. \quad (6)$$

Table 3 summarizes the computed results. MAO is more compressible than ZAO, and while at low pressure their volumes are almost equal, at elevated pressures MAO's cell becomes smaller than that of ZAO.

If the elastic constants of a solid are known, its Debye temperature can be calculated in a straightforward way [73]. At first, the longitudinal and transverse velocities of elastic waves (υ_l and υ_t) should be calculated as follows:

$$\upsilon_l = \sqrt{\frac{3B + 4G}{3\rho}}, \upsilon_t = \sqrt{\frac{G}{\rho}}, \quad (7)$$

where B is the bulk modulus, G is the shear modulus, and ρ is density. With these values, the mean velocity υ_m is calculated as

$$\upsilon_m = \left[\frac{1}{3}\left(\frac{2}{\upsilon_t^3} + \frac{1}{\upsilon_l^3}\right)\right]^{-1/3}. \quad (8)$$

Finally, the mean velocity is then used to calculate the Debye temperature Θ_D:

$$\Theta_D = \frac{h}{k}\left(\frac{3nN_A\rho}{4\pi\mu}\right)^{1/3}\upsilon_m, \quad (9)$$

where h and k are Planck's and Boltzmann's constants, respectively, N_A is Avogadro's number, μ is the molecular weight of the simulation cell, and n denotes the number of atoms in one formula unit. The calculated values of the Debye temperature in comparison with available literature data are collected in Fig. 8; the methodology of obtaining and/or

Table 5
Vibrational modes (all in cm^{-1}) for pure spinels. “R” , “IR”, and “N” stand for Raman, infrared, and no optical activity, respectively. Acoustic mode is omitted.

		MAO				ZAO	
		Experiment	this work			Experiment	this work
N	T_{2u}		278	R	T_{2g}	196[a]	209
R	T_{2g}	~300[k] 311[cj]	327	IR	T_{1u}	220–231[a]	243
IR	T_{1u}		335	N	T_{2u}		269
N	T_{1u}		347	N	T_{1u}		459
R	E_g	~400[k] 410[cj]	412	R	E_g	410[d], 420[abe]	424
N	E_u		431	N	E_u		428
N	T_{2u}		456	N	T_{2u}		464
IR	T_{1u}	481[h], 511[g]	479	IR	T_{1u}	494[l] 510[a,e]	482
R	T_{2g}	~500[k] 492[c]	571	R	T_{2g}	509[ae]	506
IR	T_{1u}	529[i], 531[f]	584	IR	T_{1u}	559[el], 574[a] 585[l]	552
N	E_u		634	N	E_u		627
IR	T_{1u}	631[g], 670[h], 690[fi]	673	IR	T_{1u}	662[l] 664[e], 684[a]	654
R	T_{2g}	671[cjk]	681	R	T_{2g}	620[d], 659[abe]	673
N	A_{2u}		687	N	A_{2u}		694
N	A_{2u}		767	N	A_{2u}		774
R	A_{1g}	772[cjk]	776	R	A_{1g}	720[b], 758[a]	783

[a] Ref.[84] ; [b] Ref.[85] ; [c] Ref.[86] ; [d] Ref.[87] ; [e] Ref.[88] ; [f] Ref.[89] ; [g] Ref.[90] ; [h] Ref.[91] ; [i] Ref.[92] ; [j] Ref.[93] ; [k] Ref.[94] ; [l] Ref.[95]

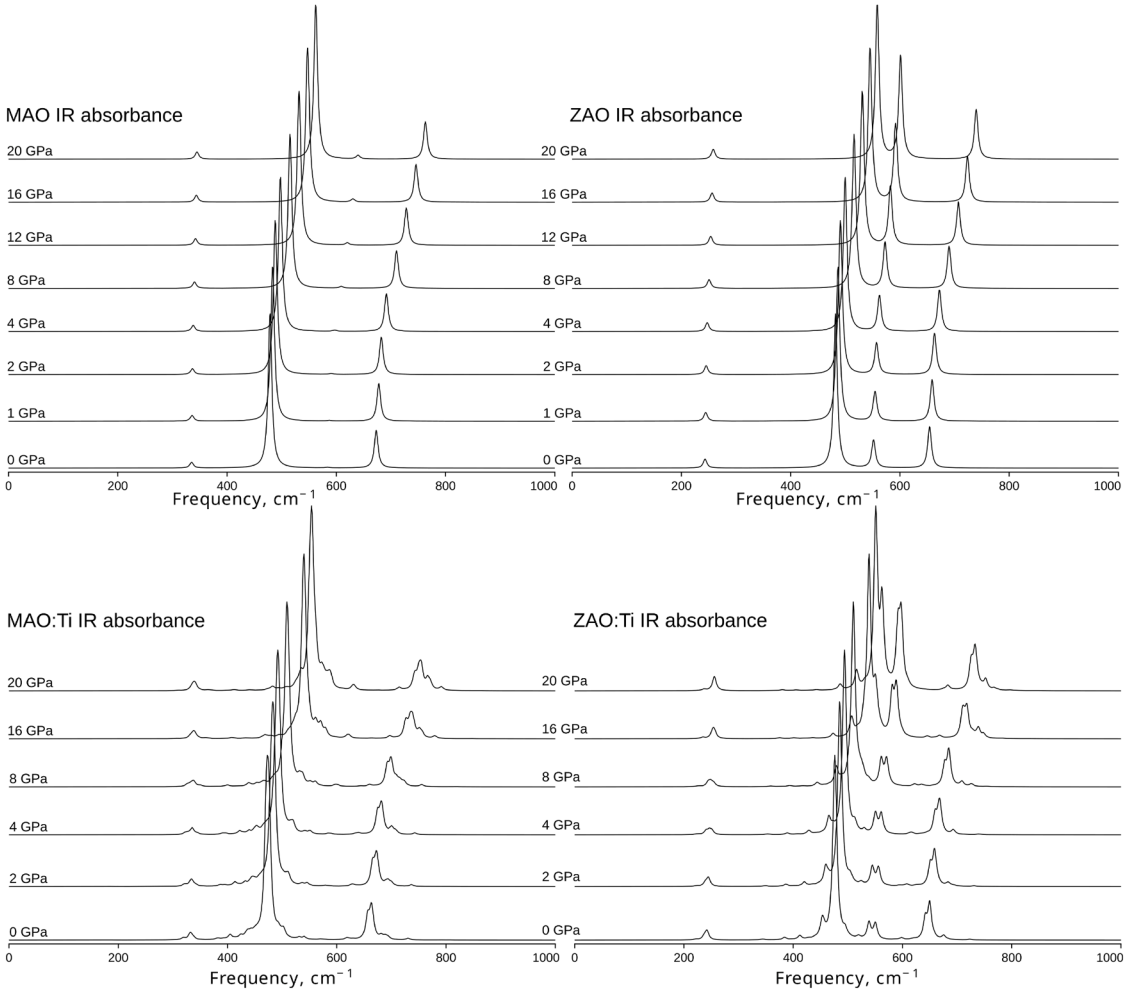

Fig. 10. Calculated IR absorbance spectra. Top row: pure spinels. Bottom row: Ti-doped spinels. Applied pressure stiffens the bonds which causes a shift to higher frequencies.

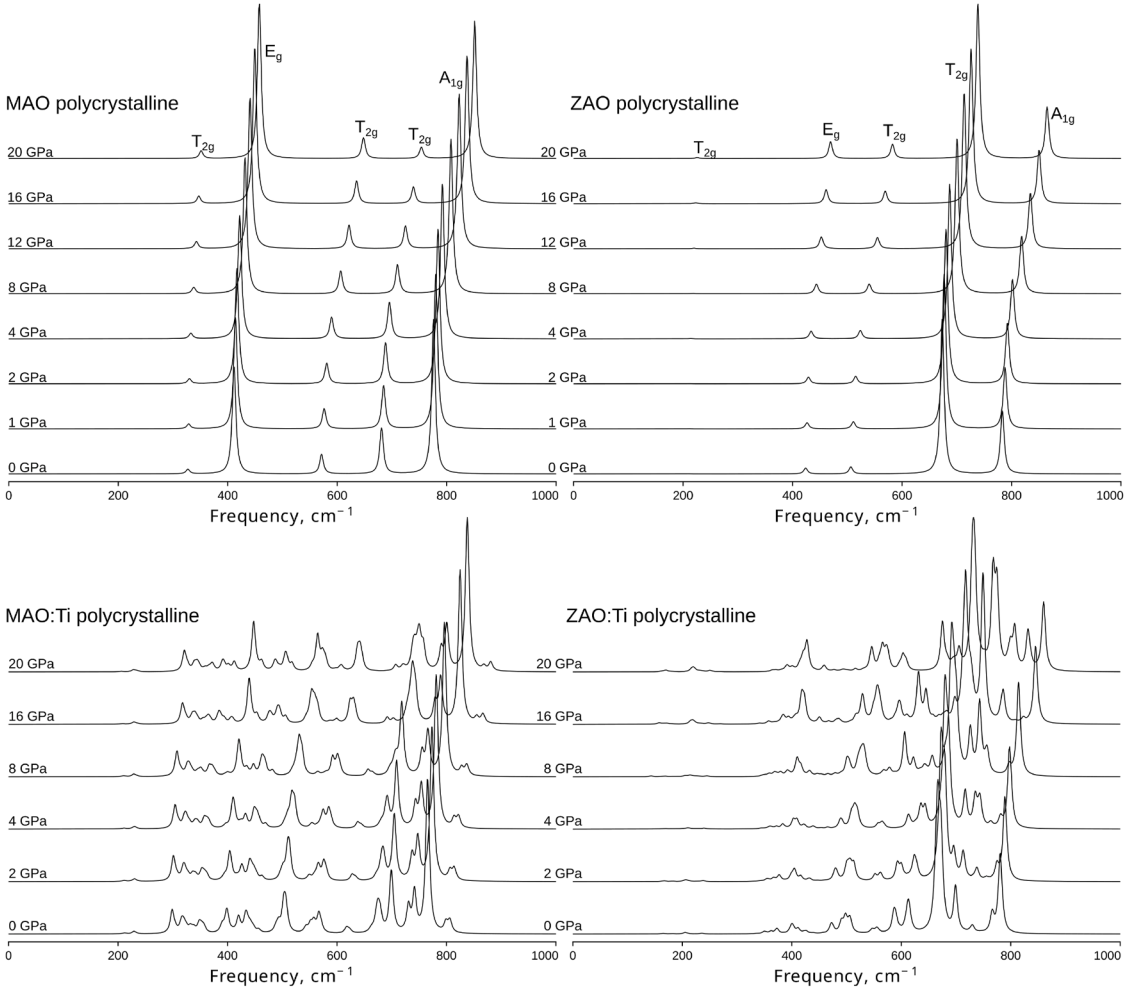

Fig. 11. Calculated Raman spectra of unoriented cells. Top row: pure spinels. Bottom row: Ti-doped spinels.

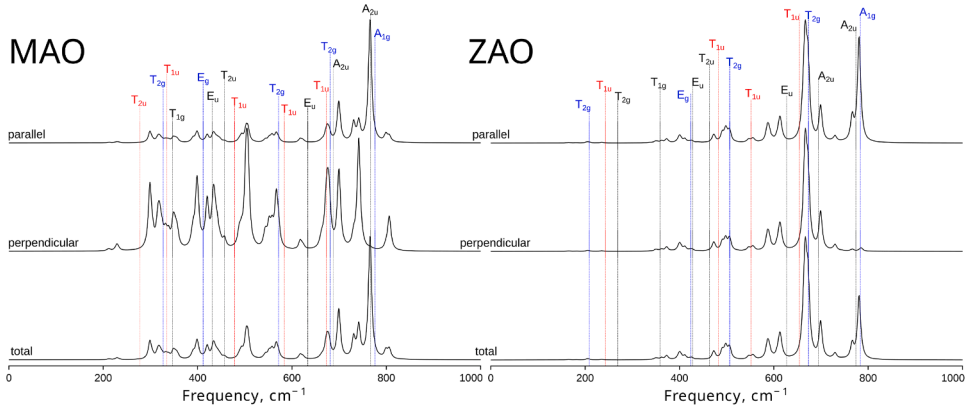

Fig. 12. Raman spectra of MAO:Ti and ZAO:Ti at 0 GPa (parallel polarisation, perpendicular polarisation, and total), overlaid with lines marking vibrational modes of pure spinels. Color of vertical lines correspond to mode's optical activity: blue for Raman, red for IR, black for optically inactive.

extracting the literature data is described in the Supporting Information. At first glance, our result (continuous yellow line in Fig. 8) looks like an overestimation wrt. experimental values. However, DFT calculations are done at T = 0K, while experimental measurements are done at much higher temperatures, and experimentally Θ_D decreases at elevated temperature [74,75]. Thus, interpolation of experimental values (e.g. lines II. and $V_{900—300K}$ in Fig. 8) places them within the confidence interval of our calculations.

Replacement of one Al ion in a unit cell by one Ti ion reduces the value of the Debye temperature by 20–40 K (Fig. 9). A slight increase of Debye temperature with pressure is observed for both neat and Ti-doped spinels.

3.5. Vibrational properties: First-principles calculations

A perfect spinel crystal with 14 atoms in a primitive unit cell has the following symmetry types of vibrational modes at the Γ point of the Brillouin zone (the size of mechanical representation is 42):

$$\Gamma_{vib} = A_{1g}(R) + E_g(R) + 3T_{2g}(R) + 5T_{1u}(IR) + T_{1g} + 2A_{2u} + 2E_u + 2T_{2u}. \quad (10)$$

Five of the nine optically active modes are Raman active, and five are IR-active. One of the IR-active T_{1u} modes is an acoustic mode, whose frequency at the Γ-point is zero. Seven modes ($2A_{2u}$, $2E_u$, T_{1g}, $2T_{2u}$) are silent i.e., they do not appear in vibrational spectra of $MgAl_2O_4$ or $ZnAl_2O_4$. Table 5 lists experimental and calculated vibrational frequencies of pure spinels.

Despite having 4 IR-active modes, experimental IR spectra of MAO have two distinct peaks in an area around 500–700 cm^{-1}. These transmittance bands are attributed to AlO_6 groups and serve as indication of spinel formation. Broad bands at ca. 3500 and 1600 cm^{-1} correspond to stretching and bending of bonds in leftover water molecules; other bands are attributed to impurities or functionalizations such as phosphate coatings [89–92]. In ZAO, depending on the range of IR measurements, 3–4 modes are observed [84,95].

Experimental Raman spectra of MAO report 4 to 6 peaks. The four principal peaks are T_{2g} at 300–311 cm^{-1}, E_g at 400–410 cm^{-1} (the most intense signal), T_{2g} at 650–670 cm^{-1}, and A_{1g} at 740–770 cm^{-1}. [93,94]. A signal between the last two peaks that appears at 720–730 cm^{-1} is assigned A_{1g} symmetry and is explained as cation inversion (redistribution of some Al ions from octahedral to tetrahedral sites) [93,94]. T_{2g} peak at 500–590 cm^{-1} is difficult to observe even in powdered samples [94]. In ZAO, 2–4 peaks are usually observed[84,85,87,88], most notably a E_g peak at ~400 cm^{-1}, and a T_{2g} peak between 600–700 cm^{-1}. Like in MAO, structural defects such as dopants and cation disorder result in additional modes.

Authors of an experimental study of Ti^{4+} impurity in $ZnAl_2O_4$ conclude that Ti "causes the infrared active T_{1u} phonons as well as the inactive phonons (T_{1g}, A_{2u}, E_u and T_{2u} symmetries) to appear in the Raman spectra" and that "replacement of aluminum atoms by titanium and zinc atoms in the Ti-doped $ZnAl_2O_4$ samples causes the loss of the symmetry and consequently the Raman spectral activity of all phonon transitions present"[84] . While it is worth noting that their samples were synthesized under Zn-rich conditions and contained Raman-detectable ZnO phase (the same fact is also reflected in their computational methodology: two Al sites in the same cell are replaced by Ti and Zn), their conclusions and their computational results agree with those yielded by our model of Ti^{3+} impurity in cubic spinels.

Figs. 10–11 show our simulated IR and Raman spectra of pure and doped spinels. Loss of local symmetry associated with Ti doping results in slight broadening of IR signals, and in a multitude of new peaks in Raman spectra. Fig. 12 shows an overlay of all vibrational modes in pure spinels over Raman spectra of Ti-doped spinels (all at 0 GPa), illustrating that while the majority of new signals in spectrum of a Ti-doped cell may indeed be interpreted as activation of pure compound's silent modes, some signals are completely new and do not correspond to decomposition of pristine multiplets.

4. Conclusions

Detailed calculations of the structural, electronic, elastic, thermodynamic and vibrational properties of the neat and Ti^{3+}-doped $MgAl_2O_4$ and $ZnAl_2O_4$ spinel crystals were performed in the present paper using the hybrid DFT approach. Due to its peculiar electron configuration ($3d^1$), the Ti^{3+} ions represent a very good model system for application of the first-principles methods in the framework of the DFT-based method, since no multielectron effects arise in the 3d electron shell. Effects of Al^{3+} substitution by Ti^{3+} were analyzed by careful examination of the changes in the electronic and structural properties upon doping.

We have shown that small distortions around Ti remove orbital degeneracy (we show that even in absence of other point defects such as vacancies or antisites, readily available in spinels, TiO_6^{9-} octahedra are easy to distort, and such distortions will enable new electronic transitions by producing additional splitting of d-states and adjusting their energies). The lowest 3d state of the Ti^{3+} is located at about 3.90 eV above the top of the valence band in MAO and 3.66 eV in ZAO, which agrees reasonably well with the corresponding calculated data for similar structural units — TiO_6^{9-} octahedra in Al_2O_3 and experimental estimations based on the analysis of the charge transfer absorption transitions for the Ti^{3+} ions in the studied hosts. Computing Ti^{3+} ground state in the band gaps of crystalline materials will help in understanding charge transfer transitions and crystal field effects on the impurity's electronic states, including crystal field splitting and local lattice deformations.

Influence of external hydrostatic pressure on the elastic constants and Debye temperature was also analyzed; linear dependencies of calculated band gaps and elastic constants on pressure were obtained in the pressure range from 0 to 20 GPa. Ti facilitates lattice dynamics in MAS and ZAS (evidenced by lower Debye temperature and activation of silent modes in Raman spectra). When one Al^{3+} ion in a unit cell is replaced by one Ti^{3+} ion, the Debye temperature is lowered by about 20–40 K, because the Ti–O chemical bonds become slightly longer and softer, if compared to the Al–O bonds. The infrared spectra of both compounds were calculated for different pressures; all prominent peaks in the spectra undergo a blue shift with applied pressure.

CRediT authorship contribution statement

Andrei Chesnokov: Writing – original draft, Visualization, Validation, Software, Investigation, Formal analysis, Data curation; **Denis Gryaznov:** Writing – original draft, Validation, Methodology, Funding acquisition, Formal analysis; **Yang Wang:** Writing – original draft, Validation, Investigation, Formal analysis; **Alise Podelinska:** Writing – original draft, Investigation, Formal analysis, Data curation; **Evgeni Shablonin:** Writing – original draft, Investigation, Formal analysis, Data curation; **Aleksandr Lushchik:** Writing – original draft, Investigation, Formal analysis, Data curation; **Pieter Dorenbos:** Writing – review & editing, Writing – original draft, Validation, Methodology, Formal analysis, Conceptualization; **Mikhail G. Brik:** Writing – review & editing, Writing – original draft, Supervision, Project administration, Investigation, Funding acquisition, Formal analysis, Conceptualization.

Data availability

Data will be made available on request.

Declaration of competing interest

The authors declare that they have no known competing financial interests or personal relationships that could have appeared to influence the work reported in this paper.

Acknowledgment

A.C. and Y.W. thank the support from the National Young Foreign Talents Plan (Grant No. Y20240231) and the Postdoctoral Foundation of Chongqing University of Posts and Telecommunications. D.G. thanks the Latvian Council of Science (grant no. lzp-2024/1-0159) for financial support. M.G.B. thanks the support from the Specialized Funding Program for the Gathering of 100 Elite Talents in Chongqing and the Overseas Talents Plan (Grant No. 2022[60]) both offered by Chongqing Association for Science and Technology, the Polish NCN

project 2021/40/Q/ST5/00336 and 2023/49/B/ST5/03384, the Estonian Research Council grant (PRG 2031), and the Ministry of Science, Technological Development, and Innovation of the Republic of Serbia under contract 451-03-47/2023-01/200017.

Supplementary material

Supplementary material associated with this article can be found in the online version at 10.1016/j.jlumin.2026.121800.

References

[1] H.S.C. O'Neill, A. Navrotsky, Simple spinels; crystallographic parameters, cation radii, lattice energies, and cation distribution, Am. Mineral. 68 (1–2) (1983) 181–194.

[2] M.G. Brik, A. Suchocki, A. Kamińska, et al., Lattice parameters and stability of the spinel compounds in relation to the ionic radii and electronegativities of constituting chemical elements, Inorg. Chem. 53 (10) (2014) 5088–5099. https://doi.org/10.1021/ic500200a

[3] Spinel, 2024, (https://www.mindat.org/min-3729.html).

[4] J. Ralph, D. Von Bargen, P. Martynov, J. Zhang, X. Que, A. Prabhu, S.M. Morrison, W. Li, W. Chen, X. Ma, Mindat.Org: The open access mineralogy database to accelerate data-intensive geoscience research, Am. Mineral. 110 (6) (2025) 833–844. https://doi.org/10.2138/am-2024-9486

[5] T.F.W. Barth, E. Posnjak, Spinel structures: with and without variate atom equipoints, Z. Kristallogr. Cryst. Mater. 82 (1–6) (1932) 325–341. https://doi.org/10.1524/zkri.1932.82.1.325

[6] K.E. Sickafus, J.M. Wills, N.W. Grimes, Structure of spinel, J. Am. Ceram. Soc. 82 (12) (1999) 3279–3292. https://doi.org/10.1111/j.1151-2916.1999.tb02241.x

[7] S. Zhongxiang, S. Jun, W. Jing, L. Yang, L. Yongfu, et al., Preparation and spectral properties of $MgAl_2O_4$: Tb^{3+} Phosphor, Spectroscopy (2023) 28–34. https://doi.org/10.56530/spectroscopy.xr3287v2

[8] M.M. Afandi, J. Kim, Full-color AC-driven electroluminescences from rare Earths-doped $ZnGa_2O_4$ in MOS structure, IEEE Electron. Device Lett. 44 (3) (2023) 484–487. https://doi.org/10.1109/LED.2023.3241217

[9] D. Valiev, S. Stepanov, V. Paygin, O. Khasanov, E. Dvilis, L. Chaolu, et al., Structural and luminescent peculiarities of spark plasma sintered transparent $MgAl_2O_4$ spinel ceramics doped with cerium ions, Inorganics 10 (10) (2022) 153. https://doi.org/10.3390/inorganics10100153

[10] M.G. Brik, J. Papan, D.J. Jovanović, M.D. Dramićanin, Luminescence of Cr^{3+} ions in $ZnAl_2O_4$ and $MgAl_2O_4$ spinels: correlation between experimental spectroscopic studies and crystal field calculations, J. Lumin. 177 (2016) 145–151. https://doi.org/10.1016/j.jlumin.2016.04.043

[11] Ž. Antić, V. Đorđević, Z. Ristić, A.M. Srivastava, W.W. Beers, M.D. Dramićanin, M.G. Brik, Influence of composition on the emission properties of impurities in solids: case study of $Mg_{1-x}Zn_xAl_2O_4$:Cr^{3+} with the spinel structure, J. Lumin. 264 (2023) 120190. https://doi.org/10.1016/j.jlumin.2023.120190

[12] Y. Wang, D. Li, Y. Yan, L. Li, G. Xiang, S. Jiang, R. Pan, X. Tang, C. Jing, X. Zhou, Y. Zhydachevskyy, A. Suchocki, Tunable and efficient broadband short-wave infrared emission of Ni^{2+}-activated spinel phosphors for advanced NIR light sources, Ceram. Int. 51 (8) (2025) 10590–10597. https://doi.org/10.1016/j.ceramint.2024.12.490

[13] P. Lombard, B. Boizot, N. Ollier, A. Jouini, A. Yoshikawa, Spectroscopic studies of Ti^{3+} ions speciation inside $MgAl_2O_4$ spinels, J. Cryst. Growth 311 (3) (2009) 899–903. https://doi.org/10.1016/j.jcrysgro.2008.09.131

[14] G. Zhang, Y. Wu, A.I. Shames, A. Goldstein, Influence of inversion level on the optical absorption spectra of Ti-doped transparent $MgGa_2O_4$ ceramics, J. Am. Ceram. Soc. 105 (9) (2022) 5944–5955. https://doi.org/10.1111/jace.18518

[15] K. Eremeev, O.S. Dymshits, I.P. Alekseeva, A. Khubetsov, M.Y. Tsenter, S. Zapalova, L. Basyrova, P.A. Loiko, A.A. Zhilin, Transparent glass-ceramics based on Ti^{3+}-doped $ZnAl_2O_4$ nanocrystals: synthesis, structure and optical properties, in: S. Taccheo, M. Ferrari, A.B. Seddon (Eds.), Fiber Lasers and Glass Photonics: Materials through Applications III, SPIE, Strasbourg, France, 2022, p. 94. https://doi.org/10.1117/12.2624442

[16] A. Lushchik, S. Dolgov, E. Feldbach, R. Pareja, A.I. Popov, E. Shablonin, V. Seeman, Creation and thermal annealing of structural defects in neutron-irradiated $MgAl_2O_4$ single crystals, Nucl. Instrum. Methods Phys. Res. B 435 (2018) 31–37. https://doi.org/10.1016/j.nimb.2017.10.018

[17] R. Dovesi, V.R. Saunders, C. Roetti, R. Orlando, C.M. Zicovich-Wilson, F. Pascale, B. Civalleri, K. Doll, N.M. Harrison, I.J. Bush, P. D'Arco, M. Llunell, M. Causà, Y. Noël, L. Maschio, A. Erba, M. Rerat, S. Casassa, B.G. Searle, J.K. Desmarais, CRYSTAL23 User's Manual, University of Torino, Torino, 2023.

[18] A. Erba, J.K. Desmarais, S. Casassa, B. Civalleri, L. Donà, I.J. Bush, B. Searle, L. Maschio, L. Edith-Daga, A. Cossard, C. Ribaldone, E. Ascrizzi, N.L. Marana, J.-P. Flament, B. Kirtman, CRYSTAL23: A program for computational solid state physics and chemistry, J. Chem. Theory Comput. 19 (20) (2023) 6891–6932. https://doi.org/10.1021/acs.jctc.2c00958

[19] A.D. Becke, Density-functional thermochemistry. III. the role of exact exchange, J. Chem. Phys. 98 (7) (1993) 5648–5652. https://doi.org/10.1063/1.464913

[20] S.H. Vosko, L. Wilk, M. Nusair, Accurate spin-dependent electron liquid correlation energies for local spin density calculations: a critical analysis, Can. J. Phys. 58 (8) (1980) 1200–1211. https://doi.org/10.1139/p80-159

[21] A. Platonenko, D. Gryaznov, E.A. Kotomin, A. Lushchik, V. Seeman, A.I. Popov, Hybrid density functional calculations of hyperfine coupling tensor for hole-type defects in $MgAl_2O_4$, Nucl. Instrum. Methods Phys. Res. B 464 (2020) 60–64. https://doi.org/10.1016/j.nimb.2019.11.046

[22] CRYSTAL Basis Sets, (https://www.crystal.unito.it/basis_sets.html).

[23] M.I. McCarthy, N.M. Harrison, *Ab initio* determination of the bulk properties of MgO, Phys. Rev. B 49 (13) (1994) 8574–8582. https://doi.org/10.1103/PhysRevB.49.8574

[24] J.E. Jaffe, A.C. Hess, Hartree-fock study of phase changes in ZnO at high pressure, Phys. Rev. B 48 (11) (1993) 7903–7909. https://doi.org/10.1103/PhysRevB.48.7903

[25] D. Gryaznov, E. Blokhin, A. Sorokine, E.A. Kotomin, R.A. Evarestov, A. Bussmann-Holder, J. Maier, A comparative *Ab initio* thermodynamic study of oxygen vacancies in ZnO and $SrTiO_3$: emphasis on phonon contribution, J. Phys. Chem. C 117 (27) (2013) 13776–13784. https://doi.org/10.1021/jp400609e

[26] A. Chesnokov, D. Gryaznov, N.V. Skorodumova, E.A. Kotomin, A. Zitolo, M. Zubkins, A. Kuzmin, A. Anspoks, J. Purans, The local atomic structure and thermoelectric properties of Ir-doped ZnO: hybrid DFT calculations and XAS experiments, J. Mater. Chem. C 9 (14) (2021) 4948–4960. https://doi.org/10.1039/D1TC00223F

[27] M. Catti, G. Valerio, R. Dovesi, M. Causà, Quantum-mechanical calculation of the solid-state equilibrium MgO + α-$Al_2O_3 \rightleftharpoons MgAl_2O_4$ (spinel) versus pressure, Phys. Rev. B 49 (20) (1994) 14179–14187. https://doi.org/10.1103/PhysRevB.49.14179

[28] M.D. Towler, N.L. Allan, N.M. Harrison, V.R. Saunders, W.C. Mackrodt, E. Aprà, *Ab initio* study of MnO and NiO, Phys. Rev. B 50 (8) (1994) 5041–5054. https://doi.org/10.1103/PhysRevB.50.5041

[29] T. Bredow, P. Heitjans, M. Wilkening, Electric field gradient calculations for Li_xTiS_2 and comparison with $_7$Li NMR results, Phys. Rev. B 70 (11) (2004) 115111. https://doi.org/10.1103/PhysRevB.70.115111

[30] F. Corà, The performance of hybrid density functionals in solid state chemistry: the case of $BaTiO_3$, Mol. Phys. 103 (18) (2005) 2483–2496. https://doi.org/10.1080/00268970500179651

[31] H.J. Monkhorst, J.D. Pack, Special points for brillouin-zone integrations, Phys. Rev. B 13 (12) (1976) 5188–5192. https://doi.org/10.1103/PhysRevB.13.5188

[32] F. Pascale, C.M. Zicovich-Wilson, F. López Gejo, B. Civalleri, R. Orlando, R. Dovesi, The calculation of the vibrational frequencies of crystalline compounds and its implementation in the CRYSTAL code: crystalline compounds and the CRYSTAL code, J. Comput. Chem. 25 (6) (2004) 888–897. https://doi.org/10.1002/jcc.20019

[33] C.M. Zicovich-Wilson, F. Pascale, C. Roetti, V.R. Saunders, R. Orlando, R. Dovesi, Calculation of the vibration frequencies of α-quartz: the effect of Hamiltonian and basis set, J. Comput. Chem. 25 (15) (2004) 1873–1881. https://doi.org/10.1002/jcc.20120

[34] W.F. Perger, J. Criswell, B. Civalleri, R. Dovesi, Ab-initio calculation of elastic constants of crystalline systems with the CRYSTAL code, Comput. Phys. Commun. 180 (10) (2009) 1753–1759. https://doi.org/10.1016/j.cpc.2009.04.022

[35] A. Erba, A. Mahmoud, D. Belmonte, R. Dovesi, High pressure elastic properties of minerals from *Ab initio* simulations: the case of pyrope, grossular and andradite silicate garnets, J. Chem. Phys. 140 (12) (2014) 124703. https://doi.org/10.1063/1.4869144

[36] S. Gražulis, D. Chateigner, R.T. Downs, A.F.T. Yokochi, M. Quirós, L. Lutterotti, E. Manakova, J. Butkus, P. Moeck, A. Le Bail, Crystallography open database – an open-access collection of crystal structures, J. Appl. Crystallogr. 42 (4) (2009) 726–729. https://doi.org/10.1107/S0021889809016690

[37] S. Gražulis, A. Daškevič, A. Merkys, D. Chateigner, L. Lutterotti, M. Quirós, N.R. Serebryanaya, P. Moeck, R.T. Downs, A. Le Bail, Crystallography open database (COD): an open-access collection of crystal structures and platform for world-wide collaboration, Nucleic Acids Res. 40 (D1) (2012) D420–D427. https://doi.org/10.1093/nar/gkr900

[38] N.G. Zorina, S.S. Kvitka, Refinement of the structure of the spinel Al_2MgO_4, Sov. Phys. Crystallogr. 13 (4) (1969) 599–600.

[39] H.St.C. O'Neill, W.A. Dollase, Crystal structures and cation distributions in simple spinels from powder XRD structural refinements: $MgCr_2O_4$, $ZnCr_2O_4$, Fe_3O_4 and the temperature dependence of the cation distribution in $ZnAl_2O_4$, Phys. Chem. Minerals 20 (8) (1994) 541–555. https://doi.org/10.1007/BF00211850

[40] H. Wondratschek, Splitting of Wyckoff positions (orbits), Mineral Petrol. 48 (2–4) (1993) 87–96. https://doi.org/10.1007/BF01163089

[41] H. Wondratschek, U. Mülller, M.I. Aroyo, I. Sens, Splitting of Wyckoff positions (orbits). II. group-subgroup chains of index 6.1, Z. Kristallogr. Cryst. Mater. 210 (8) (1995) 567–573. https://doi.org/10.1524/zkri.1995.210.8.567

[42] R.A. Evarestov, A. Platonenko, Y.F. Zhukovskii, Site symmetry approach applied to the supercell model of $MgAl_2O_4$ spinel with oxygen interstitials: Ab initio calculations, Comput. Mater. Sci. 150 (2018) 517–523. https://doi.org/10.1016/j.commatsci.2018.04.007

[43] R.A. Evarestov, D. Gryaznov, M. Arrigoni, E.A. Kotomin, A. Chesnokov, J. Maier, Use of site symmetry in supercell models of defective crystals: polarons in CeO_2, Phys. Chem. Chem. Phys. 19 (12) (2017) 8340–8348. https://doi.org/10.1039/C6CP08582B

[44] C. Freysoldt, B. Grabowski, T. Hickel, J. Neugebauer, G. Kresse, A. Janotti, C.G. Van de Walle, First-principles calculations for point defects in solids, Rev. Mod. Phys. 86 (1) (2014) 253–305. https://doi.org/10.1103/RevModPhys.86.253

[45] G.A. De Wijs, C.M. Fang, G. Kresse, G. De With, et al., First-principles calculation of the phonon spectrum of $MgAl_2O_4$ spinel, Phys. Rev. B 65 (9) (2002) 094305. https://doi.org/10.1103/PhysRevB.65.094305

[46] A. Seko, K. Yuge, F. Oba, A. Kuwabara, I. Tanaka, T. Yamamoto, First-principles study of cation disordering in Mg Al_2O_4 spinel with cluster expansion and Monte Carlo simulation, Phys. Rev. B 73 (9) (2006) 094116. https://doi.org/10.1103/PhysRevB.73.094116

[47] X. Yuan, X. Tan, B. Liu, Structural, mechanical, electronic and optical properties of spinel $ZnAl_2O_4$ underpressure from first-principles calculations, Russ. J. Phys. Chem. B 17 (4) (2023) 886–895. https://doi.org/10.1134/S1990793123040322

[48] L. Zhang, G.-F. Ji, F. Zhao, Z.-Z. Gong, First-principles study of the structural, mechanical and electronic properties of ZnX_2O_4 (X = Al, Cr and Ga), Chinese Phys. B 20 (4) (2011) 047102. https://doi.org/10.1088/1674-1056/20/4/047102

[49] F. Zerarga, A. Bouhemadou, R. Khenata, S. Bin-Omran, Structural, electronic and optical properties of spinel oxides $ZnAl_2O_4$, $ZnGa_2O_4$ and $ZnIn_2O_4$, Solid State Sci. 13 (8) (2011) 1638–1648. https://doi.org/10.1016/j.solidstatesciences.2011.06.016

[50] S. Landron, M.-B. Lepetit, Importance of $T_{2g} - e_g$ hybridization in transition metal oxides, Phys. Rev. B 77 (12) (2008) 125106. https://doi.org/10.1103/PhysRevB.77.125106

[51] C.A. Gilbert, R. Smith, S.D. Kenny, S.T. Murphy, R.W. Grimes, J.A. Ball, et al., A theoretical study of intrinsic point defects and defect clusters in magnesium aluminate spinel, J. Phys.: Condens. Matter. 21 (27) (2009) 275406. https://doi.org/10.1088/0953-8984/21/27/275406

[52] M. Rubat Du Merac, H.-J. Kleebe, M.M. Müller, I.E. Reimanis, Fifty years of research and development coming to fruition; unraveling the complex interactions during processing of transparent magnesium aluminate ($MgAl_2O_4$) spinel, J. Am. Ceram. Soc. 96 (11) (2013) 3341–3365. https://doi.org/10.1111/jace.12637

[53] K.E. Sickafus, A.C. Larson, N. Yu, M. Nastasi, G.W. Hollenberg, F.A. Garner, R.C. Bradt, et al., Cation disorder in high dose, neutron-irradiated spinel, J. Nucl. Mater. 219 (1995) 128–134. https://doi.org/10.1016/0022-3115(94)00386-6

[54] D. Bacorisen, R. Smith, B.P. Uberuaga, K.E. Sickafus, J.A. Ball, R.W. Grimes, Atomistic simulations of radiation-induced defect formation in spinels: $MgAl_2O_4$, $MgGa_2O_4$, and $MgIn_2O_4$, Phys. Rev. B 74 (21) (2006) 214105. https://doi.org/10.1103/PhysRevB.74.214105

[55] A. Lushchik, M. Kirm, A. Kotlov, P. Liblik, Ch. Lushchik, A. Maaroos, V. Nagirnyi, T. Savikhina, G. Zimmerer, Intrinsic and impurity luminescence and multiplication of excitations in complex oxides, J. Lumin. 102–103 (2003) 38–43. https://doi.org/10.1016/S0022-2313(02)00540-9

[56] G. Prieditis, E. Feldbach, I. Kudryavtseva, A.I. Popov, E. Shablonin, A. Lushchik, Luminescence characteristics of magnesium aluminate spinel crystals of different stoichiometry, IOP Conf. Ser.: Mater. Sci. Eng. 503 (2019) 012021. https://doi.org/10.1088/1757-899X/503/1/012021

[57] E. Feldbach, I. Kudryavtseva, K. Mizohata, G. Prieditis, J. Räisänen, E. Shablonin, A. Lushchik, Optical characteristics of virgin and proton-irradiated ceramics of magnesium aluminate spinel, Opt. Mater. 96 (2019) 109308. https://doi.org/10.1016/j.optmat.2019.109308

[58] M.L. Bortz, R.H. French, D.J. Jones, R.V. Kasowski, F.S. Ohuchi, Temperature dependence of the electronic structure of oxides: MgO, $MgAl_2O_4$ and Al_2O_3, Phys. Scr. 41 (4) (1990) 537–541. https://doi.org/10.1088/0031-8949/41/4/036

[59] A.V. Belyaev, I.I. Evdokimov, V.V. Drobotenko, A.A. Sorokin, A new approach to producing transparent $ZnAl_2O_4$ ceramics, J. Eur. Ceram. Soc. 37 (7) (2017) 2747–2751. https://doi.org/10.1016/j.jeurceramsoc.2017.02.041

[60] R.E. Rojas-Hernandez, F. Rubio-Marcos, I. Romet, A. Del Campo, G. Gorni, I. Hussainova, J.F. Fernandez, V. Nagirnyi, Deep-ultraviolet emitter: rare-Earth-free $ZnAl_2O_4$ nanofibers via a simple wet chemical route, Inorg. Chem. 61 (30) (2022) 11886–11896. https://doi.org/10.1021/acs.inorgchem.2c01646

[61] A.H. Reshak, S.A. Khan, Z.A. Alahmed, Investigation of electronic structure and optical properties of $MgAl_2O_4$: DFT approach, Opt. Mater. 37 (2014) 322–326. https://doi.org/10.1016/j.optmat.2014.06.017

[62] B. Amin, R. Khenata, A. Bouhemadou, I. Ahmad, M. Maqbool, Opto-electronic response of spinels $MgAl_2O_4$ and $MgGa_2O_4$ through modified Becke-Johnson exchange potential, Physica B Condens. Mat. 407 (13) (2012) 2588–2592. https://doi.org/10.1016/j.physb.2012.03.075

[63] H. Dixit, N. Tandon, S. Cottenier, R. Saniz, D. Lamoen, B. Partoens, V. Van Speybroeck, M. Waroquier, et al., Electronic structure and band gap of zinc spinel oxides beyond LDA: $ZnAl_2O_4$, $ZnGa_2O_4$ and $ZnIn_2O_4$, New J. Phys. 13 (6) (2011) 063002. https://doi.org/10.1088/1367-2630/13/6/063002

[64] M.G. Brik, Ab-initio studies of the electronic and optical properties of $Al_2O_3:Ti^{3+}$ laser crystals, Phys. B Condens. Mat. 532 (2018) 178–183. https://doi.org/10.1016/j.physb.2017.02.032

[65] P. Dorenbos, Charge transition level energies of the 1+, 2+, 3+, and 4+ $3d^q$ transition metals; new insight and tutorial review, Opt. Mater. 164 (2025) 117007. https://doi.org/10.1016/j.optmat.2025.117007

[66] P.J. Dereń, D. Stefańska, M. Ptak, M. Mączka, W. Walerczyk, G. Banach, Origin of violet-blue emission in Ti-doped gahnite, J. Am. Ceram. Soc. 97 (6) (2014) 1883–1889. https://doi.org/10.1111/jace.12858

[67] L.E. Bausá, I. Vergara, J. García-Solé, W. Strek, P.J. Deren, Laser-excited luminescence in Ti-doped $MgAl_2O_4$ spinel, J. Appl. Phys. 68 (2) (1990) 736–740. https://doi.org/10.1063/1.346807

[68] Y. Zhao, D.G. Truhlar, A new local density functional for main-group thermochemistry, transition metal bonding, thermochemical kinetics, and noncovalent interactions, J. Chem. Phys. 125 (19) (2006) 194101. https://doi.org/10.1063/1.2370993

[69] J. Sun, A. Ruzsinszky, J.P. Perdew, et al., Strongly constrained and appropriately normed semilocal density functional, Phys. Rev. Lett. 115 (3) (2015) 036402. https://doi.org/10.1103/PhysRevLett.115.036402

[70] J.W. Furness, A.D. Kaplan, J. Ning, J.P. Perdew, J. Sun, et al., Accurate and numerically efficient r^2SCAN meta-generalized gradient approximation, J. Phys. Chem. Lett. 11 (19) (2020) 8208–8215. https://doi.org/10.1021/acs.jpclett.0c02405

[71] Y. Zhao, D.G. Truhlar, The M06 suite of density functionals for main group thermochemistry, thermochemical kinetics, noncovalent interactions, excited states, and transition elements: two new functionals and systematic testing of four M06-class functionals and 12 other functionals, Theor. Chem. Acc. 120 (1–3) (2008) 215–241. https://doi.org/10.1007/s00214-007-0310-x

[72] J.P. Perdew, A. Ruzsinszky, G.I. Csonka, O.A. Vydrov, G.E. Scuseria, L.A. Constantin, X. Zhou, K. Burke, et al., Restoring the density-gradient expansion for exchange in solids and surfaces, Phys. Rev. Lett. 100 (13) (2008) 136406. https://doi.org/10.1103/PhysRevLett.100.136406

[73] O.L. Anderson, A simplified method for calculating the debye temperature from elastic constants, J. Phys. Chem. Solids 24 (7) (1963) 909–917. https://doi.org/10.1016/0022-3697(63)90067-2

[74] V. Askarpour, M.H. Manghnani, S. Fassbender, A. Yoneda, Elasticity of single-crystal $MgAl_2O_4$ spinel up to 1273 K by Brillouin spectroscopy, Phys. Chem. Miner. 19 (8) (1993) 511–519. https://doi.org/10.1007/BF00203051

[75] Y. Zou, S. Gréaux, T. Irifune, B. Li, Y. Higo, Unusual pressure effect on the shear modulus in $MgAl_2O_4$ spinel, J. Phys. Chem. C 117 (46) (2013) 24518–24526. https://doi.org/10.1021/jp404901a

[76] H.-P. Liu, R.N. Schock, D.L. Anderson, Temperature dependence of single-crystal spinel ($MgAl_2O_4$) elastic constants from 293 to 423°K measured by light-sound scattering in the Raman-Nath region, Geophys. J. Int. 42 (1) (1975) 217–250. https://doi.org/10.1111/j.1365-246X.1975.tb05858.x

[77] I. Suzuki, M. Kumazawa, Anomalous thermal expansion in spinel $MgAl_2O_4$: a possibility for a second order phase transition?, Phys. Chem. Miner. 5 (3) (1980) 279–284. https://doi.org/10.1007/BF00348575

[78] Z.P. Chang, G.R. Barsch, Pressure dependence of single-crystal elastic constants and anharmonic properties of spinel, J. Geophys. Res. 78 (14) (1973) 2418–2433. https://doi.org/10.1029/JB078i014p02418

[79] Materials Data on $MgAl_2O_4$ by materials project, 2020, https://doi.org/10.17188/1206986

[80] A. Jain, S.P. Ong, G. Hautier, W. Chen, W.D. Richards, S. Dacek, S. Cholia, D. Gunter, D. Skinner, G. Ceder, K.A. Persson, Commentary: the materials project: a materials genome approach to accelerating materials innovation, APL Mater. 1 (1) (2013) 011002. https://doi.org/10.1063/1.4812323

[81] M. De Jong, W. Chen, T. Angsten, A. Jain, R. Notestine, A. Gamst, M. Sluiter, C. Krishna Ande, S. Van Der Zwaag, J.J. Plata, C. Toher, S. Curtarolo, G. Ceder, K.A. Persson, M. Asta, Charting the complete elastic properties of inorganic crystalline compounds, Sci. Data 2 (1) (2015) 150009. https://doi.org/10.1038/sdata.2015.9

[82] Y. Duan, X. Li, N. Sun, H. Ni, S.N. Tkachev, Z. Mao, et al., Single-crystal elasticity of $MgAl_2O_4$-Spinel up to 10.9 GPa and 1000 K: implication for the velocity structure of the top upper mantle, Earth Planet. Sci. Lett. 481 (2018) 41–47. https://doi.org/10.1016/j.epsl.2017.10.014

[83] H.J. Reichmann, Sound velocities and elastic constants of $ZnAl_2O_4$ spinel and implications for spinel-elasticity systematics, Am. Mineral. 91 (7) (2006) 1049–1054. https://doi.org/10.2138/am.2006.2122

[84] V. Mohaček-Grošev, M. Vrankić, A. Maksimović, V. Mandić, Influence of titanium doping on the raman spectra of nanocrystalline $ZnAl_2O_4$, J. Alloys Compd. 697 (2017) 90–95. https://doi.org/10.1016/j.jallcom.2016.12.116

[85] D. Dwibedi, C. Murugesan, M. Leskes, P. Barpanda, Role of annealing temperature on cation ordering in hydrothermally prepared zinc aluminate (ZnAl2O4) spinel, Mater. Res. Bull. 98 (2018) 219–224. https://doi.org/10.1016/j.materresbull.2017.10.010

[86] D. Simeone, C. Dodane-Thiriet, D. Gosset, P. Daniel, M. Beauvy, Order–disorder phase transition induced by swift ions in $MgAl_2O_4$ and $ZnAl_2O_4$ spinels, J. Nucl. Mater. 300 (2–3) (2002) 151–160. https://doi.org/10.1016/S0022-3115(01)00749-8

[87] Y. Sun, J. Xu, R. Xi, H. Zhang, L. Liu, X. Xu, X. Fang, X. Wang, Unraveling the intrinsic reasons promoting the reactivity of $ZnAl_2O_4$ spinel by Fe and Co for CO oxidation, Catal. Surv. Asia 25 (2) (2021) 180–191. https://doi.org/10.1007/s10563-021-09324-w

[88] Y. Chen, J. Zheng, M. Lu, Z. Liu, Z. Zhou, Gemological and spectral characteristics of gem-quality blue gahnite from Nigeria, J. Spectrosc. 2024 (2024) 1–9. https://doi.org/10.1155/2024/6693346

[89] J. Guo, H. Lou, H. Zhao, X. Wang, X. Zheng, Novel synthesis of high surface area $MgAl_2O_4$ spinel as catalyst support, Mater. Lett. 58 (12–13) (2004) 1920–1923. https://doi.org/10.1016/j.matlet.2003.12.013

[90] M.F. Zawrah, H. Hamaad, S. Meky, Synthesis and characterization of nano $MgAl_2O_4$ spinel by the co-precipitated method, Ceram. Int. 33 (6) (2007) 969–978. https://doi.org/10.1016/j.ceramint.2006.02.015

[91] C.T. Mathew, S. Solomon, J.K. Thomas, Structural, optical and vibrational characterization of infrared - transparent nanostructured $MgAl_2O_4$ synthesized by a modified combustion technique, Mater. Today Proc. 2 (3) (2015) 954–958. https://doi.org/10.1016/j.matpr.2015.06.015

[92] S. Sanjabi, A. Obeydavi, Synthesis and characterization of nanocrystalline $MgAl_2o_4$ spinel via modified sol–gel method, J. Alloys Compd. 645 (2015) 535–540. https://doi.org/10.1016/j.jallcom.2015.05.107

[93] H. Cynn, S.K. Sharma, T.F. Cooney, M. Nicol, High-temperature Raman investigation of order-disorder behavior in the $MgAl_2O_4$ spinel, Phys. Rev. B 45 (1) (1992) 500–502. https://doi.org/10.1103/PhysRevB.45.500

[94] N. Obradovic, S. Filipovic, W. Fahrenholtz, B. Marinkovic, J. Rogan, S. Levic, A. Djordjevic, V. Pavlovic, Morphological and structural characterization of $MgAl_2O_4$ spinel, Sci. Sinter. 55 (1) (2023) 1–10. https://doi.org/10.2298/SOS2301001O

[95] A.A. Da Silva, A. De Souza Gonçalves, M.R. Davolos, Characterization of nanosized $ZnAl_2O_4$ spinel synthesized by the sol–gel method, J. Sol-Gel Sci. Technol. 49 (1) (2009) 101–105. https://doi.org/10.1007/s10971-008-1833-x